International Journal of Heat and Mass Transfer 228 (2024) 125605

Contents lists available at ScienceDirect

International Journal of Heat and Mass Transfer

journal homepage: www.elsevier.com/locate/ijhmt

Full-scale numerical simulations of standing-wave thermoacoustic engines with circular-pore and pin-array stacks

Geng Chen [a,*,1], Shancheng Tao [a,1], Kai Wang [a], Lihua Tang [b,*], Zhaoyu Li [c,d], Jingyuan Xu [e], Zhibin Yu [f]

[a] National Engineering Research Center of Power Generation Control and Safety, School of Energy and Environment, Southeast University, Nanjing 210096, China
[b] Department of Mechanical Engineering, University of Auckland, 20 Symonds Street, Auckland 1010, New Zealand
[c] China Railway Eryuan Engineering Group Co., Ltd., Beijing 100039, China
[d] School of Computing and Artificial Intelligence, Southwest Jiaotong University, Chengdu 611756, China
[e] Institute of Microstructure Technology, Karlsruhe Institute of Technology, Karlsruhe 76344, Germany
[f] Department of Mechanical and Aerospace Engineering, University of Liverpool, Liverpool L69 3BX, UK

ARTICLE INFO

Keywords:
Thermoacoustic engine
Computational fluid dynamics
Circular pores
Pin arrays
Vortex shedding
Low-grade heat recovery

ABSTRACT

Thermoacoustic engines (TAEs) can convert thermal energy into acoustic energy with no moving parts. Previous numerical studies normally focused on the TAEs with a parallel-plate stack due to their simple structures and used two-dimensional (2-D) computational fluid dynamics (CFD) models to save computational costs. In this study, we conduct full-scale three-dimensional (3-D) CFD simulations on the standing-wave TAEs with more complicated circular-pore and pin-array stacks. Firstly, the dynamic behavior of the standing-wave TAEs in the start-up process is investigated. It is found that the optimal ratios of hydraulic radius r_h to thermal penetration depth δ_k for the TAEs with circular-pore and pin-array stacks are 2 and 3.2, respectively. Secondly, the acoustic, hydrodynamic, and thermodynamic characteristics of the standing-wave TAEs in the steady-state process are explored. We find that when operating at optimal r_h/δ_k, the TAE with a pin-array stack generates much larger acoustic power than that with a circular-pore stack. Examination of the vortex shedding at the stack ends indicates that the pin arrays exhibit less flow resistance than circular pores. At optimal r_h/δ_k, the time-averaged transversal heat flux at the pin array ends is calculated to be around 1.2×10^5 W/m^2, which is larger than 7.5×10^4 W/m^2 of circular pores, corresponding to a better thermodynamic performance. The 3-D numerical investigations in this work give deeper insights into the performances of TAEs with circular-pore and pin-array stacks which were investigated in experiments, providing useful guidance for the future design and development of more sophisticated thermoacoustic devices for low-grade heat recovery.

1. Introduction

Thermoacoustic engines (TAEs) are novel thermally-driven machines that can convert thermal energy into acoustic energy based on the thermoacoustic effect [1–3]. In TAEs, the compressible fluid such as air, argon, or helium, contracts and expands while exchanging heat with the inhomogeneously heated porous material, forming a thermodynamic cycle and leading to self-excited acoustic oscillations [4–6]. Generally, a TAE is composed of two main parts: a "thermoacoustic core" and an acoustic resonator. The thermoacoustic core consists of a pair of hot and cold (or ambient) heat exchangers and a porous material (sandwiched between the heat exchangers) [7] while the acoustic resonator serves as a waveguide for the propagation of acoustic waves [8]. TAEs can be classified into standing-wave and travelling-wave types. The standing-wave TAEs which usually own a linear acoustic resonator, are simpler in structure but less efficient in power generation than the travelling-wave TAEs that normally possess a looped acoustic resonator. TAEs have gained widespread attention in recent years because they have no mechanical moving parts, environmentally friendly working fluids, and flexible heat source options [9–11].

The porous material, usually named "stack" in the standing-wave TAEs, has some typical structures, including parallel plates [12], circular pores [13], pin arrays [14], etc. Among the various stacks, parallel

* Correspondent authors.
E-mail addresses: chengeng@seu.edu.cn (G. Chen), l.tang@auckland.ac.nz (L. Tang).
[1] These authors contribute equally to the paper.

https://doi.org/10.1016/j.ijheatmasstransfer.2024.125605
Received 7 February 2024; Received in revised form 13 April 2024; Accepted 20 April 2024
Available online 30 April 2024

Nomenclature

A_{fluid}	cross-sectional area of fluid channels (m^2)
c_p	specific heat at constant pressure (J/kg·K)
D	tube diameter (m)
f	frequency (Hz)
I	acoustic power (W)
k	turbulent kinetic energy (J)
L_H	hot buffer length (m)
L_R	resonator length (m)
L_S	stack length (m)
p	pressure (Pa)
q_t	time-averaged heat flux (W/m^2)
r_0	pore radius (m)
r_h	hydraulic radius (m)
r_p	pin radius (m)
S	cross-section
T	temperature (K)
u	velocity (m/s)
y	pore/pin distance (m)

Greek symbols

λ	thermal conductivity (W/m·K)
δ_k	thermal penetration depth (m)
κ	thermal diffusivity (m^2/s)
μ	dynamic viscosity (kg/s·m)
ρ	density (kg/m^3)
σ	Prandtl number
ω	angular frequency (rad/s)
ε	turbulent dissipation rate
$\mathbf{\Omega}$	vorticity rate tensor

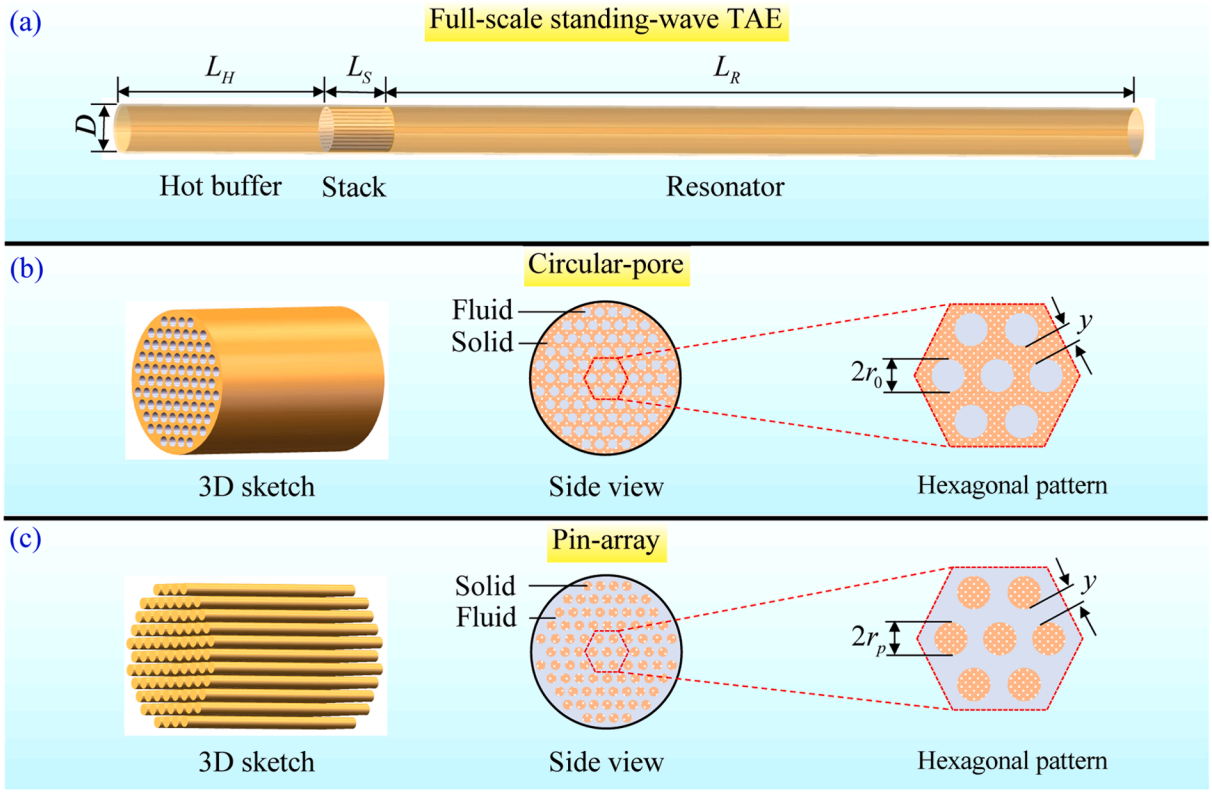

Fig. 1. (a) 3-D model of the standing-wave TAE. (b) 3-D sketch of the circular-pore stack and side view. (c) 3-D sketch of the pin-array stack and side view.

plates are widely studied in the literature since they have a simple geometry and are easy to fabricate [15–17]. The gap between parallel plates plays a pivotal role in the thermal-acoustic energy conversion. Previous studies indicate that for parallel plates, the optimal value of r_h/δ_k for achieving the lowest onset temperature is around 1.5, with r_h being the hydraulic radius (i.e., half of the gap) and δ_k being the thermal penetration depth, respectively [18–20]. Compared with parallel plates, stacks composed of circular pores or pin arrays are more complicated in geometry and therefore less investigated. Previous studies on circular-pore stacks [21–23] or pin-array stacks [24] normally focused on spatial-average functions and heat transfer characteristics through theoretical analysis and experimental measurements. It was found that TAEs with a pin-array stack generally own superior performances than TAEs employing stacks of other types [25].

Another method that is commonly utilized to investigate thermoacoustic stack is computational fluid dynamics (CFD) [26–28]. CFD simulations can provide more detailed and accurate information than physical experiments and offer a deeper understanding of the flow behavior within the TAE. Nevertheless, CFD simulations on TAEs can be computationally expensive and time-consuming because of (1) the large space scales ranging from 10^{-4} m (the order of magnitude of the thermal penetration depth) to 1 m (the order of magnitude of the total length) [29] and (2) the large time scales ranging from 10^{-5} s (i.e., the timestep size) to 1 s (the order of magnitude of the flow time) [30]. To save computational cost, simplifications were made in previous research, including (1) choosing parallel plates as the stack type due to their

Table 1
Dimensions of major components in the TAEs.

	TAE with a circular-pore stack		TAE with a pin-array stack	
Fixed parameters	Tube diameter D	21 mm	Tube diameter D	21 mm
	Hot buffer length L_H	100 mm	Hot buffer length L_H	100 mm
	Stack length L_S	30 mm	Stack length L_S	30 mm
	Resonator length L_R	370 mm	Resonator length L_R	370 mm
	Pore distance y	0.5 mm	Pin distance y	0.5 mm
Changing variables	Pore radius r_0	0.6 to 1.2 mm	Pin radius r_p	0.5 to 0.8 mm
Dimensionless quantity	r_h/δ_k	1.5 to 3	r_h/δ_k	4.2 to 1.78

simple structure [31], (2) truncating the computational domain around the stack [32], and (3) carrying out two-dimensional (2-D) simulations [33]. However, in most cases, the results calculated from those simplified models cannot present the practical operating conditions of TAEs, in particular for TAEs with circular-pore or pin-array stacks. Hence, improvements should be made to the existing 2-D simplified models to more accurately simulate the intricate phenomena of all kinds in different TAEs.

To fill the research gap mentioned above, this study performs full-scale three-dimensional (3-D) CFD simulations on quarter-wavelength standing-wave TAEs with circular-pore and pin-array stacks. High-performance computing is employed to facilitate multiple calculations of CFD tasks and significantly reduce the running time. Based on the simulation results, the characteristics of standing-wave TAEs in the start-up and steady-state processes including natural frequency, growth rate, acoustic pressure, velocity, acoustic power, vorticity, heat flux, etc., are described in detail. The outline of this article is organized as follows. Section 2 develops full-scale 3-D TAE models and introduces the CFD simulation procedure. Section 3 analyses the dynamic behavior of TAEs in the initial start-up process. Section 4 characterizes the TAEs working at steady state from different perspectives. Finally, several key conclusions are summarized in Section 5.

2. Numerical methodology

2.1. Model description

Fig. 1(a) depicts the 3-D models of the standing-wave TAEs with circular-pore and pin-array stacks investigated in this study. The TAEs consist of a stack of length L_S located at a distance L_H from the left end and a resonator tube of diameter D and length L_R. The stack, which is the core component of the TAE, ensures a large thermal contact area between the working fluid and solid stack, thus remarkably enhancing the acoustic power generation. The hot buffer closed at the left end and the resonator opened at the right end contribute to a quarter-wavelength standing wave inside the TAE. To save computational cost, heat exchangers at the ends of the stack are not modelled. Figs. 1(b) and 1(c) illustrate 3-D sketches of the circular-pore and pin-array stacks. For the circular-pore stack, the hollow circular pores of radius r_0 are arranged in a hexagonal pattern [34] and filled with working fluid, which is ambient air in this study. For the pin-array stack, solid pins of radius r_p are distributed in a hexagonal pattern and the working fluid flows between them. In both figures, the distance between adjacent pins or circular pores is defined by y.

In this study, the dimensionless quantity r_h/δ_k reflecting the perfectness of thermal contact between the oscillatory fluid and still solid is adopted to investigate the effect of stack parameters on the performance of TAEs. The hydraulic radius r_h is defined by V_{fluid} / A_{wet}, where V_{fluid} is the volume of working fluid and A_{wet} is the wet perimeter. r_h for circular pores and pin arrays are calculated by

$$\begin{cases} r_h = r_0/2, \text{circular pores} \\ r_h = \left(D^2/4 - nr_p^2\right)/\left(2nr_p + D\right), \text{pin arrays} \end{cases} \quad (1)$$

where D is the tube diameter and n denotes the number of circular pores or pins. The thermal penetration depth δ_k indicates how far heat from the solid can diffuse laterally into the working fluid. It is expressed by

$$\delta_k = \sqrt{2\kappa/\omega} \quad (2)$$

where κ is the thermal diffusivity of the working fluid, and ω is the angular frequency. To change r_h/δ_k, we alter the values of r_0 and r_p while

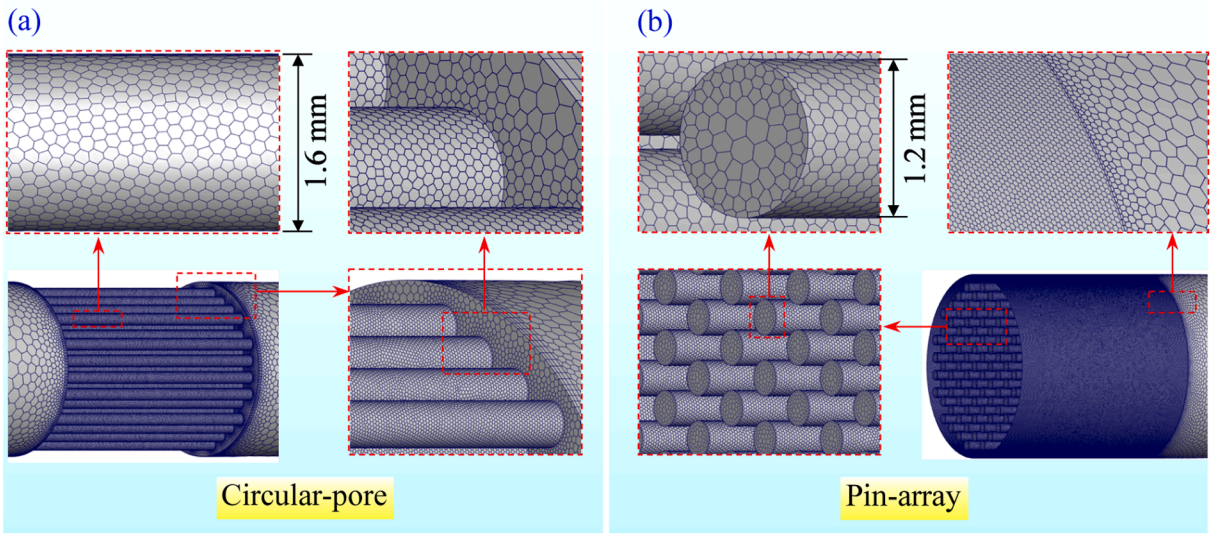

Fig. 2. 3-D meshing of (a) the circular-pore stack and (b) the pin-array stack.

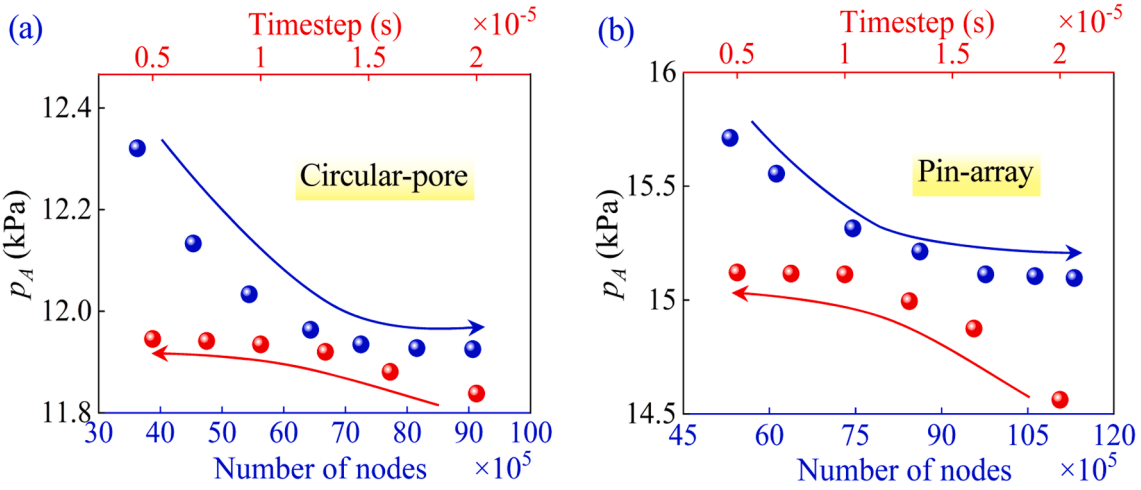

Fig. 3. Sensitivity study of mesh and time step sizes. (a) TAE with a circular-pore stack and (b) TAE with a pin-array stack.

keeping other stack parameters unchanged, as shown in Table 1. For the circular-pore stack, r_0 changes from 0.6 mm to 1.2 mm with an increment of 0.1 mm. Accordingly, r_h/δ_k increases from 1.5 to 3. For the pin-array stack, r_p varies from 0.5 mm to 0.8 mm with an increment of 0.05 mm. Accordingly, r_h/δ_k decreases from 4.2 to 1.78.

2.2. Simulation procedures

2.2.1. Pre-processing

As the first step in CFD simulations, pre-processing involves geometry modeling and mesh generation. Firstly, the 3-D models of the TAEs with circular-pore and pin-array stacks are constructed in the CAD (Computer-Aided Design) software SolidWorks, as shown in Fig. 1. Secondly, structured meshes are generated for the 3-D models in ICEM CFD that divides the computational domain into discrete elements. The mesh details of the circular-pore and pin-array stacks are presented in Fig. 2. It is worth noting that the meshes in the stack flow channels should be much denser than those in the hot buffer and resonator, which is an important setting for realizing self-excited thermoacoustic oscillations in CFD simulations. The total number of nodes for the TAE with a circular-pore stack (r_0 = 0.8 mm) is 7,251,195, which is less than 9,766,872 for the TAE with a pin-array stack (r_p = 0.6 mm). To calculate such high numbers of nodes, high-performance computing is resorted, and it takes around 40 days to reach the final steady state using parallel processing with 32 CPUs (1 G memory per CPU) for each calculation task.

2.2.2. Iteration

Following pre-processing, several iterative schemes are implemented to arrive at the converged simulation results.

(1) *Setting of the boundary conditions*. The left end of the hot buffer is set as a rigid wall having a temperature of 900 K, while the right end of the resonator is defined as a pressure outlet with a gauge pressure of 0 Pa. No-slip conditions are enforced on the walls of the hot buffer and resonator, whose temperatures are maintained at 900 K and 300 K, respectively. A linear temperature distribution decreasing from T_H at the left end to T_C at the right end is imposed on the stack walls using a User Defined Function (UDF).

(2) *Definition of the properties of the working fluid*. It is assumed that the working fluid inside the TAE is air at ambient pressure satisfying the equation of state $p = \rho R_g T$ for an ideal gas, where p, ρ, and R_g represent the pressure, density, and specific gas constant, respectively. The working fluid is also compressible and satisfies the three-dimensional Navier-Stokes equations

$$\frac{\partial \rho}{\partial t} + \frac{\partial(\rho u_i)}{\partial x_i} = 0 \tag{3}$$

$$\frac{\partial(\rho u_i)}{\partial t} + \frac{\partial(\rho u_i u_j)}{\partial x_i} = \frac{\partial \sigma_{ij}}{\partial x_j} - \frac{\partial p}{\partial x_i} \tag{4}$$

$$\frac{\partial(\rho e_t)}{\partial t} + \frac{\partial(\rho u_i e_t)}{\partial x_i} = -\frac{\partial(\rho u_i)}{\partial x_i} + \frac{\partial(\sigma_{ij} u_i)}{\partial x_i} - \frac{\partial}{\partial x_i}\left(\lambda\left(\frac{\partial T}{\partial x_i}\right)\right) \tag{5}$$

where u, λ, and e denote the velocity, thermal conductivity, and internal energy. σ_{ij} is the stress tensor for Newtonian viscous fluid, expressed by

$$\sigma_{ij} = 2\mu S_{ij} - \frac{2}{3}\mu \frac{\partial u_k}{\partial x_k}\delta_{ij} \tag{6}$$

where μ, S_{ij}, and δ_{ij} are dynamic viscosity, strain-rate tensor, and Kronecker delta. i, j, and k denote indices of the coordinates. Specifically, the strain-rate tensor S_{ij} can be described by

$$S_{ij} = \frac{1}{2}\left(\frac{\partial u_j}{\partial x_i} + \frac{\partial u_i}{\partial x_j}\right) \tag{7}$$

The thermal conductivity λ of the working fluid is defined using the kinetic theory,

$$\lambda = \frac{15}{4}\frac{R}{M_w}\mu\left(\frac{4}{15}\frac{c_p M_w}{R} + \frac{1}{3}\right) \tag{8}$$

where R is the universal gas constant, M_w is the molecular weight, and c_p is the specific heat capacity. The dynamic viscosity μ obeys the power law

$$\mu = \mu_0 (T/T_0)^b \tag{9}$$

where reference viscosity μ_0, reference temperature T_0, and temperature exponent b are set as 1.85×10^{-5} kg/m·s, 300 K, and 0.76, respectively.

(3) *Selection of appropriate numerical schemes and algorithms*. In this work, ANSYS Fluent is chosen as the CFD solver. The PISO (Pressure-Implicit Splitting Operators) scheme is selected for pressure-velocity coupling, the second-order upwind approach is employed for spatial discretization, and the second-order implicit algorithm is adopted for temporal discretization. To simulate and predict the behavior of turbulent flows, the widely used standard k-ε model is adopted in this study [35–37]. The standard k-ε

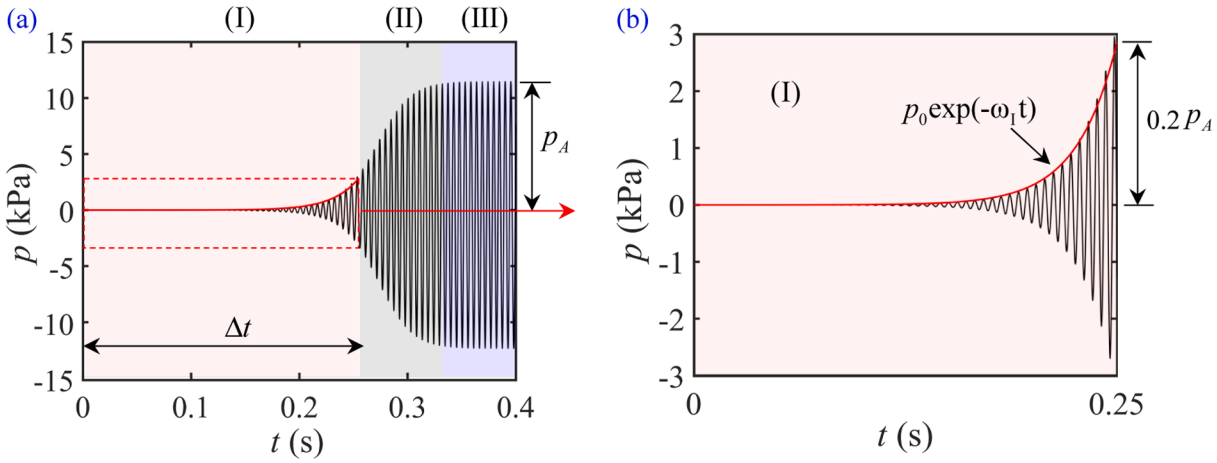

Fig. 4. (a) Evolution of acoustic pressure at the left end of the thermoacoustic engine with a circular-pore stack (r_0 = 0.8 mm) at T_H = 900 K; (b) Enlarged view of pressure oscillations in the start-up process.

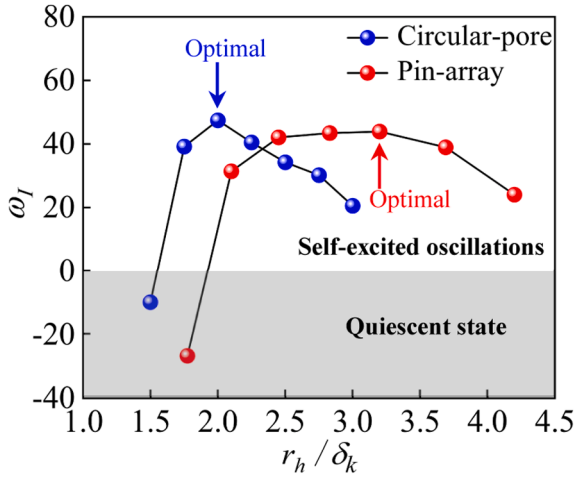

Fig. 5. Effect of r_h/δ_k on ω_I for TAEs with circular-pore and pin-array stacks.

model is relatively computationally efficient and suitable for a wide range of turbulent flows. It contains two transport equations

$$\frac{\partial}{\partial t}(\rho k)+\frac{\partial}{\partial x_i}(\rho k u_i)=\frac{\partial}{\partial x_j}\left[\left(\mu+\frac{\mu_t}{\sigma_k}\right)\frac{\partial k}{\partial x_j}\right]+G_k-\rho\varepsilon+S_k \tag{10}$$

$$\frac{\partial}{\partial t}(\rho \varepsilon)+\frac{\partial}{\partial x_i}(\rho \varepsilon u_i)=\frac{\partial}{\partial x_j}\left[\left(\mu+\frac{\mu_t}{\sigma_\varepsilon}\right)\frac{\partial \varepsilon}{\partial x_j}\right]+C_{1\varepsilon}G_k\frac{\varepsilon}{k}-C_{2\varepsilon}\rho\frac{\varepsilon^2}{k}+S_\varepsilon \tag{11}$$

where G_k, S_k and S_ε are turbulence kinetic energy, the source term for the turbulent kinetic energy k and the source term for the turbulent dissipation rate ε, respectively. The turbulence viscosity μ_t can be expressed as

$$\mu_t=\rho C_\mu\frac{k^2}{\varepsilon} \tag{12}$$

C_μ, σ_k, σ_ε, $C_{1\varepsilon}$ and $C_{2\varepsilon}$ in Eqs. (11) and (12) are five constants with their values being 0.09, 1.00, 1.30, 1.44 and 4.92, respectively.

(4) *Configuration of initial conditions*. In the solution initialization, the initial values of the gauge pressure and temperature at the pressure outlet are set at 0.1 Pa and 300 K, whereas other variables such as velocity, turbulence kinetic energy, and turbulent dissipation rate are set at zero. Thereafter, we start the solver iterations for the transient flow calculation with a timestep size of 10^{-5} s.

2.2.3. Post-processing

Post-processing commences after the convergence of solutions is achieved in the iteration process. The first important task in post-processing is quality checks that involve sensitivity studies of both the grid size and timestep size. In the grid size sensitivity study, we examined 7 meshes with different numbers of nodes for the TAEs with a circular-pore stack (r_0 = 0.8 mm) and a pin-array stack (r_p = 0.6 mm). The timestep size is chosen as 10 μs. Fig. 3(a) shows that the pressure amplitude p_A at the closed end decreases and asymptotes as the number of nodes increases from 3,627,559 to 7,251,195 for the TAE with a circular-pore stack. Further increasing the number of nodes leads to negligible changes (less than 0.1 %) in the pressure amplitude. Therefore, the optimal number of nodes for the TAE with a circular-pore stack is chosen as 7,251,195. Likewise, as depicted in Fig. 3(b), the optimal number of nodes for the TAE with a pin-array stack is found to be 9,766,872. In the timestep size sensitivity study, we examined 6 timestep sizes ranging from 5 μs to 20 μs. The optimal numbers of nodes are selected. It is found that at large timestep sizes, thermoacoustic oscillations cannot occur. The pressure increases and asymptotes as the timestep size decreases towards 5 μs. To achieve a tradeoff between the accuracy of simulation results and the computational costs, the optimal timestep size is chosen as 10 μs.

Following the quality checks, variables of interest (including pressure, velocity, temperature, etc.) at different locations are processed to characterize the TAEs with circular-pore and pin-array stacks. Attention is paid to the performances of TAEs in the start-up and steady-state processes, which will be analyzed and discussed in Section 3 and Section 4.

3. Dynamic behavior in the start-up process

When the temperature at the stack ends is above the critical temperature, the working fluid inside the TAE spontaneously transits from a stationary state to periodic oscillations. Take the TAE with the circular-pore stack (r_0 = 0.8 mm) as an example. As shown in Fig. 4(a), the evolution of acoustic pressure at the left end can be divided into three stages: (I) *Start-up process*. In this process, the acoustic power generated in the stack exceeds the dissipations in the hot buffer and resonator. Consequently, the acoustic pressure is amplified with its amplitude growing exponentially with time. (II) *Saturation*. In this process, the pressure amplitude continues to increase and levels off because the dissipation increases nonlinearly at large amplitudes. (III) *Limit-cycle*

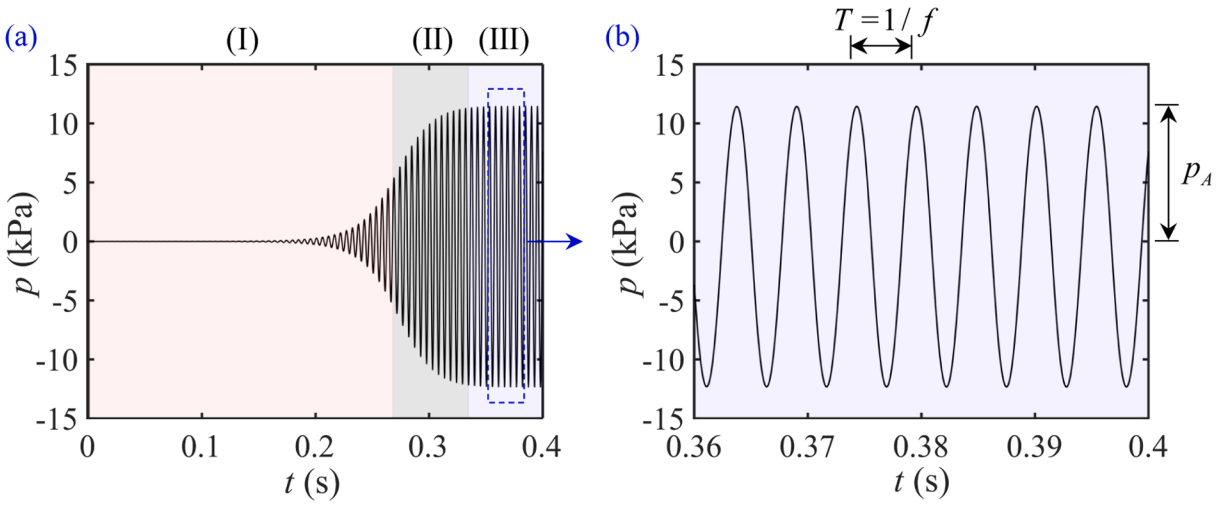

Fig. 6. (a) Time history of pressure fluctuations at the left end of the TAE with a circular-pore stack; (b) Limit-cycle oscillations at steady state. In the calculations, T_H is fixed at 900 K.

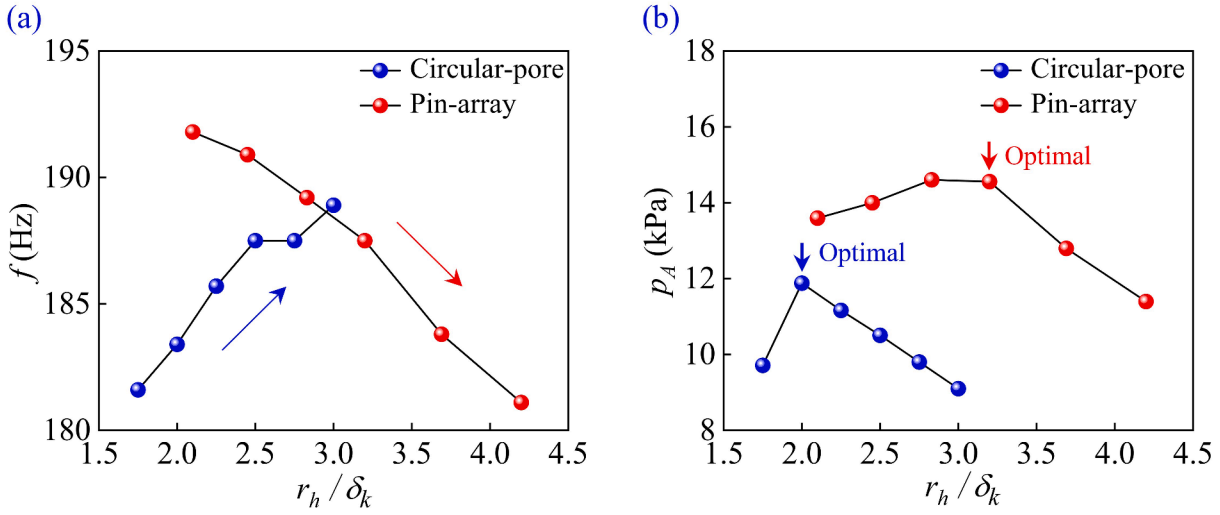

Fig. 7. Effect of r_h/δ_k on natural frequency f and pressure amplitude p_A for TAEs with circular-pore and pin-array stacks. In the calculations, T_H is fixed at 900 K.

oscillations. In this process, the TAE oscillates at a constant pressure amplitude. A dynamic equilibrium is achieved between the acoustic power generation and dissipations at the steady state.

The dynamic behavior of the TAE in the start-up process is further explored in detail, as shown in Fig. 4(b). By examining the time history of acoustic pressure from 0 to 0.25 s (reaching 20 % of the amplitude at steady state), we notice that the envelope of instantaneous pressure oscillations in the start-up process can be expressed by

$$p(t) = p_0 e^{(-\omega_I t)} \tag{13}$$

where p_0 and ω_I denote the reference amplitude and growth rate, respectively. Fig. 5 plots the dependence of growth rates of TAEs with circular-pore and pin-array stacks on r_h/δ_k. It can be seen that in both cases, ω_I first increases and then decreases as r_h/δ_k increases. For the TAE with a circular-pore stack, ω_I reaches the maximum value of 47.42 when r_h/δ_k is 2 whereas for the TAE with a pin-array stack, ω_I reaches the maximum value of 43.91 when r_h/δ_k is 3.2. A larger ω_I means that the TAE can reach limit-cycle oscillations at a faster speed. From the stability viewpoint, a larger ω_I reveals that TAE is more unstable at $T_H =$ 900 K, indicating a lower onset temperature at this specific r_h/δ_k. Hence, the optimal r_h/δ_k for achieving the lowest onset temperature difference for TAEs with circular-pore and pin-array stacks are 2 and 3.2, respectively. It is also interesting to note that, r_h/δ_k has optimal values because the standing-wave TAEs reply on imperfect thermal contact between the oscillatory fluid and still solid. When r_h/δ_k is too small or large, the thermal contact is either perfect or negligible, which are both not favorable for producing acoustic power. In such cases, ω_I has negative values, representing attenuation of pressure oscillations, and spontaneous acoustic oscillations will not occur inside the TAEs.

The growth rate ω_I can also be estimated theoretically using a reduced-order network model based on linear thermoacoustic theory. Comparisons are made between the theoretical and numerical results for TAEs with circular-pore and pin-array stacks at different T_H. Detailed analysis can be found in the Appendix.

4. Performances at steady state

4.1. Natural frequency and pressure amplitude

Limit-cycle oscillations (in stage III) are observed after the TAE reaches the steady state after saturation. Fig. 6(a) presents the time-domain signal of acoustic pressure at the left end of the TAE with a circular-pore stack. It can be seen from the limit-cycle oscillations in

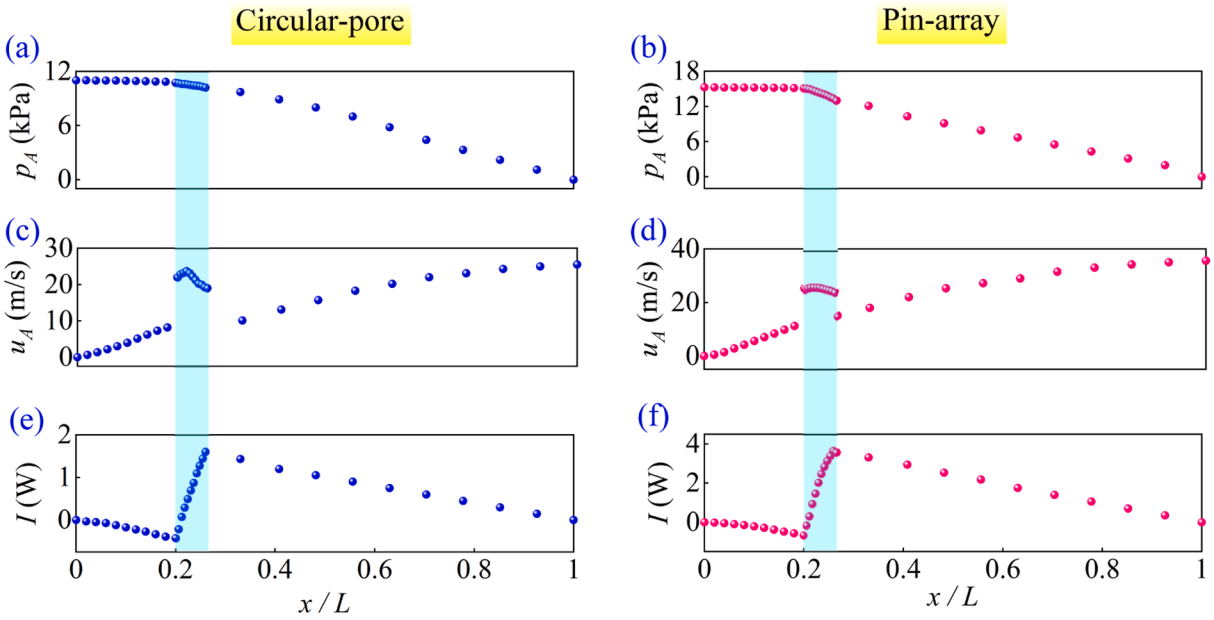

Fig. 8. Distributions of acoustic pressure, velocity, and acoustic power for TAEs with circular-pore and pin-array stacks. The TAEs operate at optimal r_h/δ_k of 2 and 3.2, respectively.

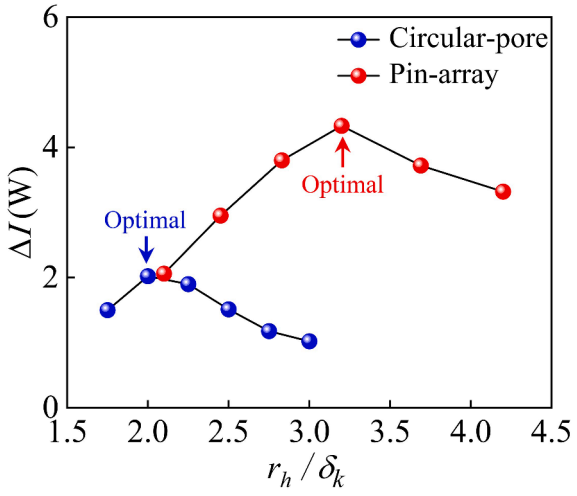

Fig. 9. Effect of r_h/δ_k on the acoustic power generation ΔI in the circular-pore and pin-array stacks. In the calculations, T_H is fixed at 900 K.

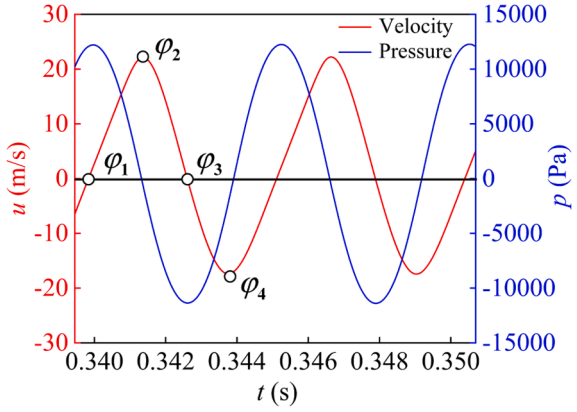

Fig. 10. Waveforms of velocity and pressure in two acoustic cycles.

Fig. 6(b) that the TAE oscillates sinusoidally at a natural frequency f of 183.75 Hz with a constant pressure amplitude p_A of 11,902 Pa. Figs. 7(a) and 7(b) illustrate f and p_A of the TAEs with circular-pore and pin-array stacks, respectively. In the calculations, r_h/δ_k varies while T_H is fixed at 900 K. From Fig. 7(a), we can see that f of the TAE with a circular-pore stack increases with increasing r_h/δ_k while f of the TAE with a pin-array stack exhibits an opposite trend. To explain this, we have to first understand that f of the TAE increases with the increase of the porosity of the stack [1]. As seen in Fig. 1, for the circular-pore stack, a larger r_h/δ_k corresponds to a larger r_0, which indicates a larger porosity and a higher f. Nonetheless, for the pin-array stack, a larger r_h/δ_k corresponds to a larger r_p, which indicates a smaller porosity and a smaller f. It can be noticed from Fig. 7(b) that p_A peaks at r_h/δ_k of 2 and 3.2 respectively for TAEs with circular-pore and pin-array stacks. The optimal values of r_h/δ_k for maximum p_A are consistent with those for maximum ω_I in Fig. 5. The maximum p_A for the TAEs with a pin-array stack is 15,113 Pa which is larger than 11,902 Pa for the TAEs with a circular-pore stack.

4.2. Distributions of pressure, velocity, and acoustic power

To have a complete picture of the acoustic field inside the TAE, axial distributions of pressure amplitude p_A, velocity amplitude u_A, and acoustic power I are investigated. The acoustic power I, which represents the capability of doing work, is expressed by

$$I = \frac{\omega}{2\pi} \oint puA_{fluid}\, dt \tag{14}$$

where A_{fluid} denotes the cross-sectional area of fluid channels. Fig. 8 displays the distributions of p_A, u_A, and I for the TAEs with circular-pore and pin-array stacks operating at optimal r_h/δ_k of 2 and 3.2, respectively. In both TAEs, standing waves dominate inside the linear tubes with the pressure antinode and the velocity node being at the left end, and the pressure node and the velocity antinode being at the right end. The velocity amplitude changes abruptly at the stack ends due to the sudden increase or decrease of A_{fluid} in the stack region. The acoustic power, being zero at the left end, first decreases in the hot buffer, then increases in the stack region (i.e., the area shaded in blue), and finally decreases in the resonator (to zero at the right end). By comparing Figs. 8(a) and 8(b), we find that in the stack region, p_A drops more in the TAE with a pin-

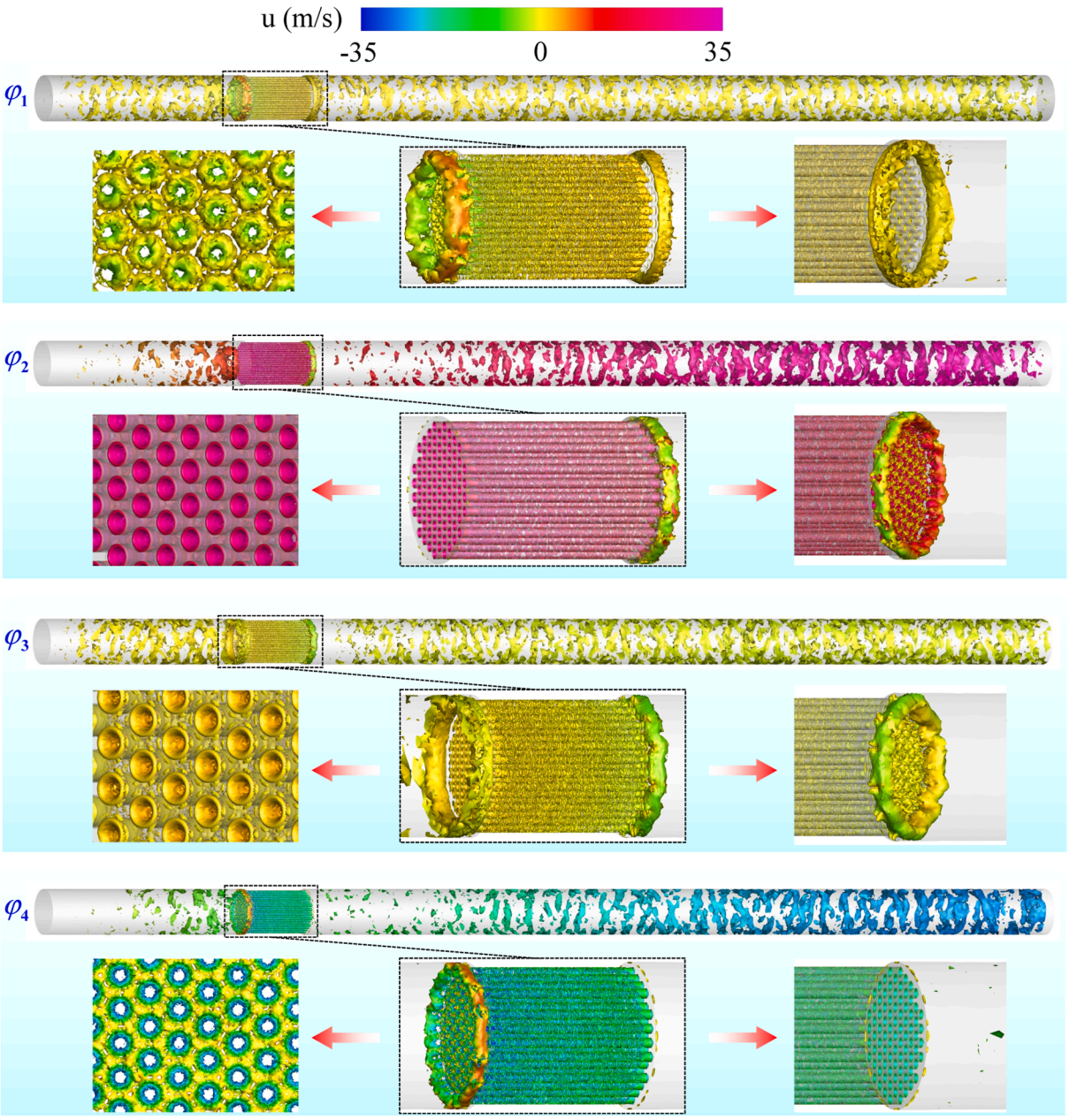

Fig. 11. Vortices inside the TAE with a circular-pore stack at four different instants at $T_H = 900$ K.

array stack, indicating a stronger impact of acoustic inertance. In contrast, I increases more in the stack region for the TAE with a pin-array stack, representing larger acoustic power generation because of the thermoacoustic effect.

Fig. 9 plots the difference ΔI between acoustic power at the stack ends versus r_h/δ_k for the TAEs with circular-pore and pin-array stacks. In the calculations, T_H is fixed at 900 K. The results show that at optimal r_h/δ_k of 2 and 3.2, ΔI reaches maximum values of 2.02 W and 4.27 W, respectively. From the figure, we can tell that the ΔI of pin arrays is two times larger than that of circular pores. Moreover, for the TAE with a pin-array stack, even at r_h/δ_k that deviates from its optimal value, ΔI is still larger than the maximum ΔI by the circular-pore stack. This demonstrates that compared with the circular-pore stack, the pin-array stack usually has a superior performance in thermal-acoustic energy conversion. According to Swift [1], the pin array has a larger Im[$-f_k$] as compared to circular pores (see page 99, Im[] denotes the imaginary part of a complex quantity), while Im[$-f_k$] is important for acoustic power in standing-wave TAEs (see page 124). This explains why the pin array is more efficient than circular pores in producing acoustic power.

4.3. Vortices and velocity streamlines

It is also interesting to investigate the oscillatory flows inside the TAE operating at the steady state. Fig. 10 shows the waveforms of space-averaged pressure and velocity in the middle of the circular-pore stack (i.e., $x = 0.115$ mm) with a r_h/δ_k of 2 at $T_H = 900$ K. Four instants of interest during one acoustic cycle are selected: φ_1 and φ_3 are moments at which the velocity is zero, while φ_2 and φ_4 are moments at which the velocity is maximum and minimum. Figs. 11 and 12 illustrate the vortex inside the TAEs with circular-pore and pin-array stacks at four instants (φ_1, φ_2, φ_3, and φ_4). The Q-criterion is used to identify multiscale vortices in the flow field, which is described as

$$Q = \frac{1}{2}\left(|\boldsymbol{\Omega}|^2 - |\mathbf{S}|^2\right) \tag{15}$$

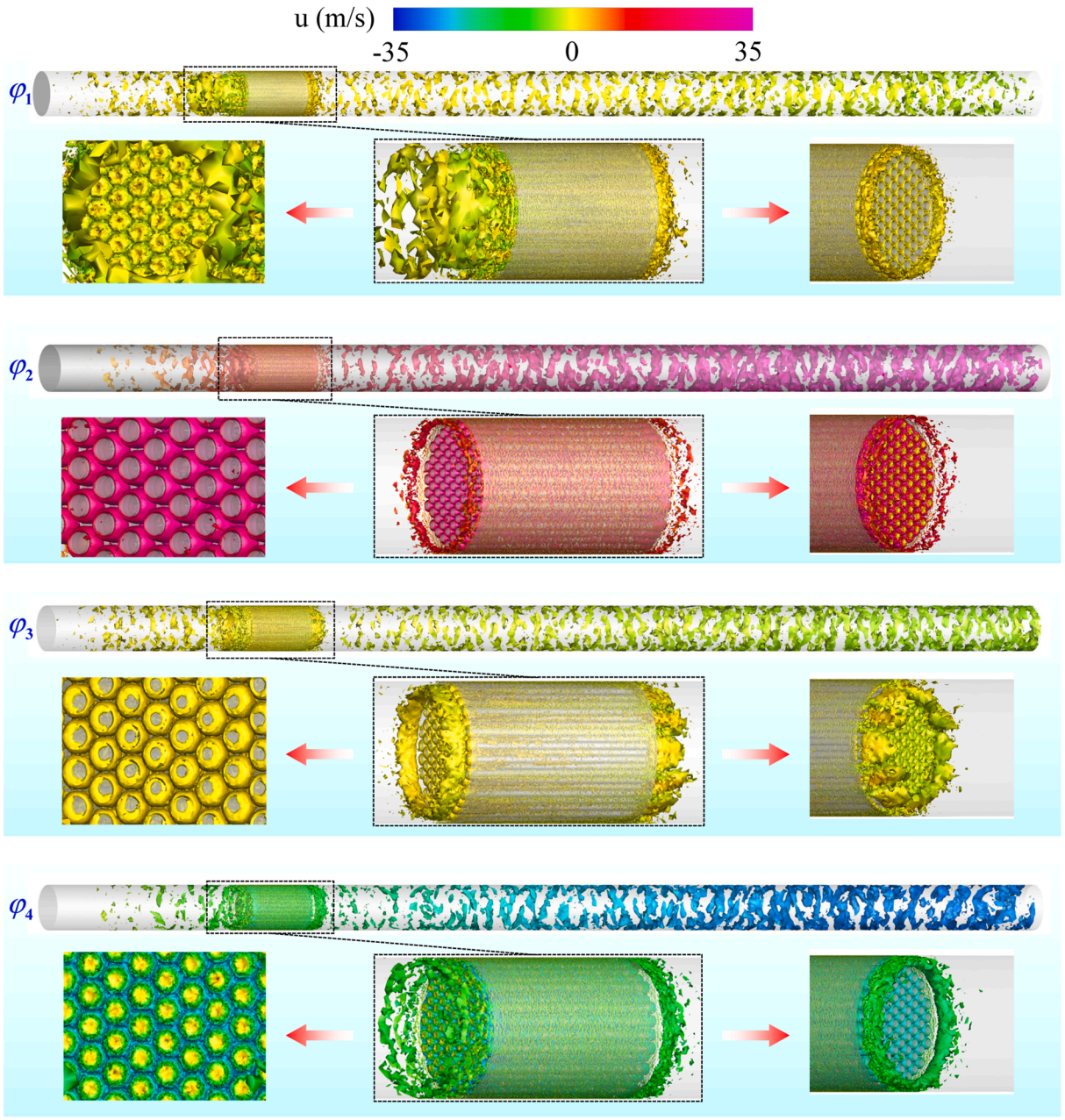

Fig. 12. Vortices inside the TAE with a pin-array stack at four different instants at $T_H = 900$ K.

where **Ω** and **S** denote the vorticity rate tensor and strain rate tensor, respectively. In the figures, Q of 10,000 is chosen and the vortex is colored by the magnitude of instantaneous velocity. It can be seen that due to the viscosity of the working fluid, discontinuous spiral vortices show up at the wall surfaces of the hot buffer and resonator. The vortices are stronger at the right end of the resonator, which is consistent with the higher velocity at that location. At the ends of the stack, vortex shedding along the x-axis direction is observed due to the sudden decrease in the cross-sectional area. This brings about additional viscous losses (so-called minor losses [38]) that restrict the increase of pressure amplitude.

The patterns of vortices at the ends of circular-pore and pin-array stacks are different. For the TAE with a circular-pore stack, at instants φ_1 and φ_3, large ring vortices are observed around its periphery. These ring vortices arise because of the circular flows as visualized by the velocity streamlines in Fig. 13(a). Besides, small toroidal vortex rings are observed at the ends of circular pores. At instant φ_2, the velocity reaches a maximum and the working fluid flows along the x-axis in the forward direction. No significant vortices are observed at the left end, while large eddies and evident circular flows can be seen at the right end. On the contrary, at the instant φ_4, the velocity reaches a maximum and the working fluid flows along the x-axis in the backward direction. Large eddies and obvious circular flows are found at the left end.

For the TAE with a pin-array stack, at instants φ_1 and φ_3, a large number of vortices are observed near the stack ends as evidenced by the circular flows near the pin ends in Fig. 13(b). At instants φ_2 and φ_4, the kinetic energy of the fluid is high, no circular flows are found at either end of the pin arrays, and the vortices break down in the flow directions. This feature is different from the circular-pore stack where circular flows can be found at one end at instant φ_2 or φ_4 (i.e., maximum velocities). Hence, we can infer that the pin-array stack has a smaller flow resistance than the circular-pore stack.

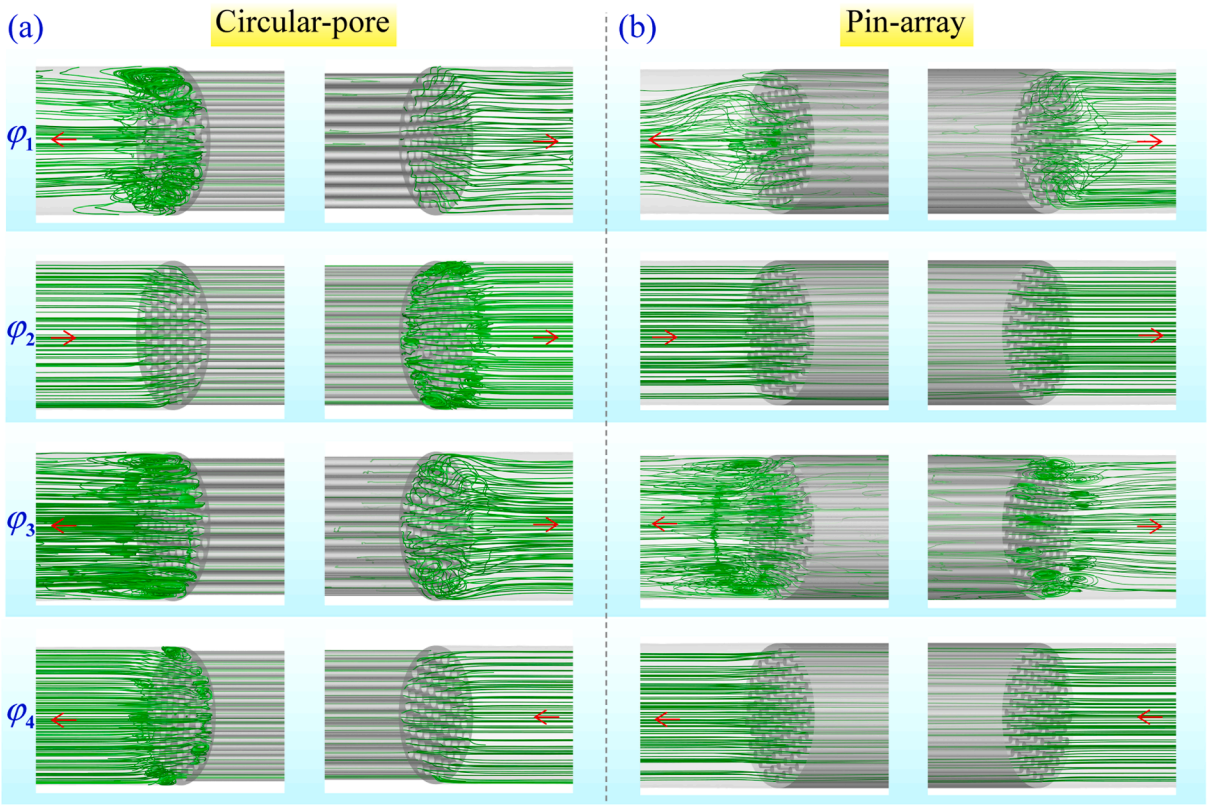

Fig. 13. Velocity streamlines around the (a) circular-pore stack and (b) pin-array stack at four different instants at $T_H = 900$ K. The direction of the arrow indicates the direction of flow.

4.4. Heat transportation

Heat transportation in standing-wave TAEs happens in both longitudinal and transversal directions. Longitudinal heat transportation usually occurs at the stack ends because of vortex shedding while transversal heat transportation takes place at the surfaces of solid stacks.

To visualize the longitudinal heat transportation, one cross section S_0 centered by the tube axis, and six cross sections S_1 to S_6 perpendicular to the tube axis are selected, as shown in Fig. 14(a). Figs. 14(b) and 14(c) display the time-averaged temperature contours of the selected cross sections. In Fig. 14(b), a small zone colder than 900 K is observed near the left end of the stacks while a small zone warmer than 300 K is found near the right end of the stacks. These "heat leaks" [1] are mainly attributed to the shedding of vortices that transport heat from the stack to the hot buffer or resonator in the longitudinal direction. Heat leaks will reduce the TAE efficiency since the heat leaked outside the stack is not involved in thermal-acoustic energy conversion. In Fig. 14(c), we can see that the relatively "colder" or "warmer" vortices coming from the stack channels break down into small eddies as they enter the hot buffer or resonator. Therefore, the cross sections that are away from the stack ends have a more uniform mean temperature. We also notice that at the same locations (e.g., S_3 and S_4), the mean temperature is more uniform for the pin-array stack, demonstrating a better mixing performance.

Transversal heat transportation at the stack wall surfaces can be estimated using time-averaged heat flux, which is defined as

$$q_t = -\kappa \frac{\partial T_m}{\partial n}\bigg|_{surface} = h(T_w - T_m) \tag{16}$$

where T_w, T_m, h, and n denote the wall temperature, the space-averaged mean temperature, the surface heat transfer coefficient, and the direction of the perpendicular wall, respectively. Fig. 15 displays the contours of time-averaged heat flux at surfaces of the circular-pore and pin-array stacks. It can be seen that q_t is positive at the left end but negative at the right end. This indicates that the working fluid absorbs heat from the left part of the stack but releases heat to the right part of the stack. By comparing Figs. 15(a) and 15(b), we find that $|q_t|$ is larger at the ends for the pin-array stack, indicating stronger transversal heat transportation. It is interesting to note that, for the circular-pore stack, q_t is larger at the ends of circular pores in the center rather than at the periphery. This implies that more working fluid flows through the circular pores in the center of the stack. However, for the pin-array stack, q_t is larger at the ends of pins at the periphery, indicating more working fluid flowing between the pins at the periphery of the stack.

According to the first law of thermodynamics, the difference between the heat absorption Q_{in} and heat release Q_{out} in the stack region approximates the acoustic power ΔI, i.e.,

$$\sum \int_{0.1}^{0.13} q_{t,si} \Pi_{si} dx = Q_{in} - Q_{out} \approx \Delta I \tag{17}$$

where $q_{t,si}$ and Π_{si} denote the transversal heat fluxes and perimeters of circular pores or pins. Fig. 16 further plots q_t of circular pores and pin arrays. It can be seen that $q_{t,si}$ of circular pores and pin arrays intersect with $q_t = 0$ at around $x = 0.118$ m and $x = 0.115$ m, respectively. This means that a relatively larger proportion of circular pores serves as the "hot heat exchanger" in traditional standing-wave TAEs with heat exchangers. Using Eq. (17), ΔI of the circular-pore stack and pin-array stack are calculated to be 1.72 W and 3.83 W, respectively. These results are 14.8 % and 11.5 % smaller than those reported in Fig. 9 using Eq. (14). The reason behind the deviations primarily lies in the heat leaks that reduce the amount of thermal energy to be converted into acoustic power.

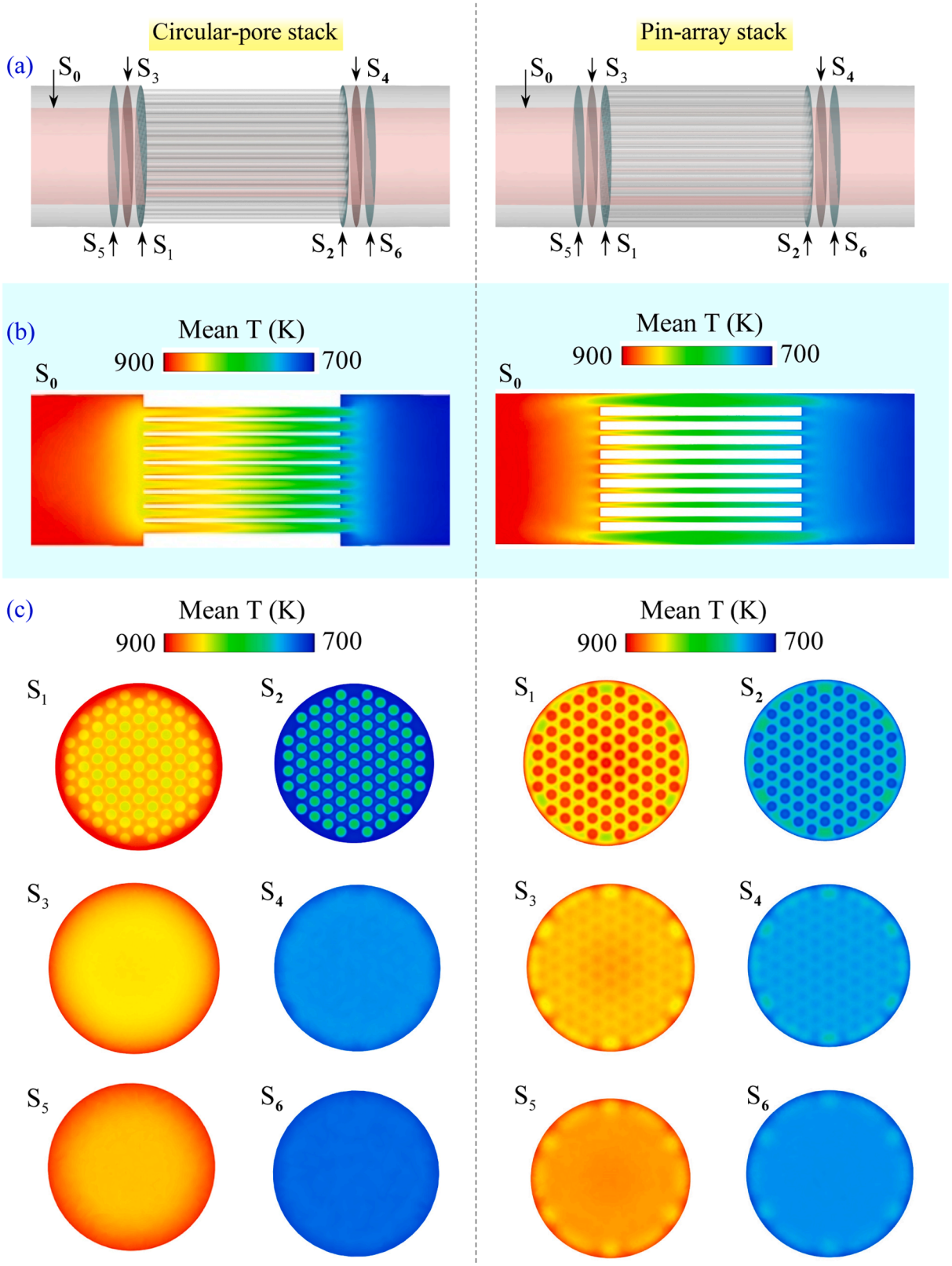

Fig. 14. Contours of time-averaged temperature around circular-pore and pin-array stacks.

5. Conclusions

In this work, full-scale three-dimensional (3-D) numerical simulations are carried out on the quarter-wavelength standing-wave thermoacoustic engines (TAEs) with circular-pore and pin-array stacks. High-quality structured meshes are generated for the 3-D models and high-performance computing (HPC) is employed to facilitate the calculations. First, the dynamic behavior of the TAEs with different stack parameters in the start-up process is simulated via computational fluid dynamics (CFD) and validated against linear thermoacoustic theory.

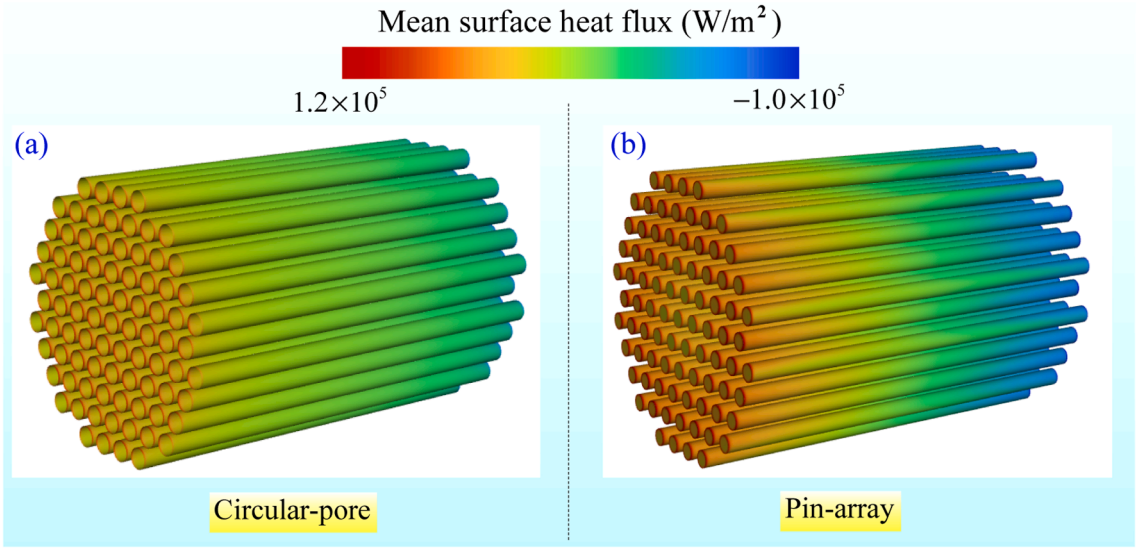

Fig. 15. Contours of time-averaged transversal heat flux at the surfaces of the (a) circular-pore stack and (b) pin-array stack.

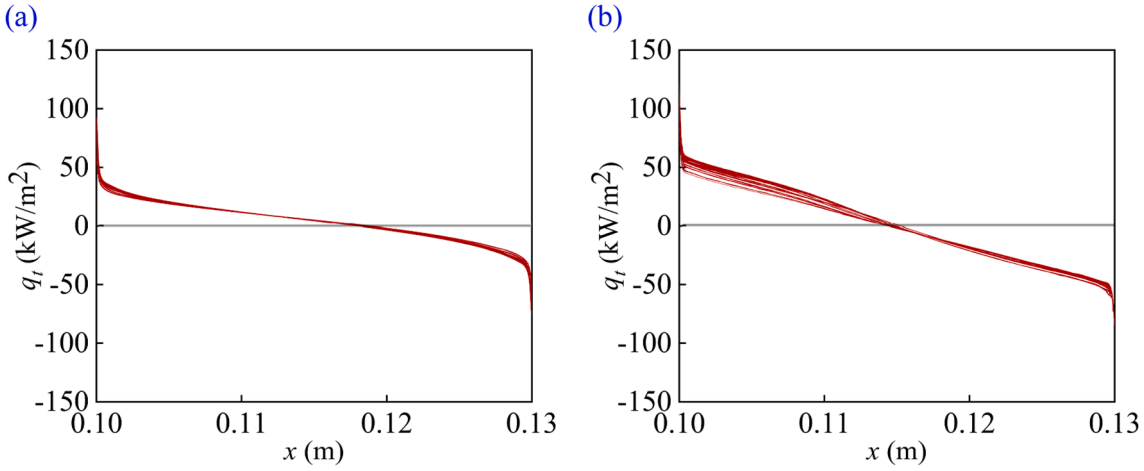

Fig. 16. Time-averaged transversal heat fluxes of (a) circular pores and (b) pin arrays.

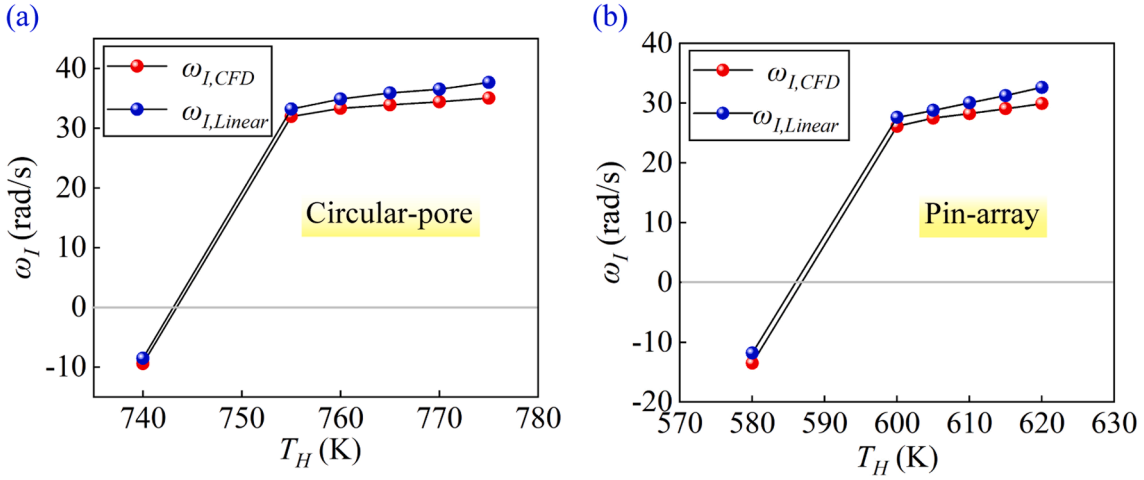

Fig. 17. Comparisons between numerical and theoretical results of TAE with (a) a circular-pore stack and (b) a pin-array stack.

Thereafter, the steady-state performances of TAEs working at optimal r_h/δ_k are analyzed and discussed from multiple perspectives. The main conclusions can be drawn as follows.

(1) In the start-up process, the acoustic pressure is amplified with its amplitude p_A growing exponentially with time at a growth rate ω_I that is dependent on the stack parameters or specifically r_h/δ_k. For TAE with circular-pore and pin-array stacks, the optimal r_h/δ_k for achieving the maximum ω_I are 2 and 3.2, respectively.
(2) At the steady state, the maximum pressure amplitude p_A and acoustic power generation ΔI are also achieved at optimal r_h/δ_k of 2 and 3.2. In particular, the maximum p_A and ΔI for the TAE with a pin-array stack are much larger than those of a circular-pore stack. The pin-array stack performs better in thermal-acoustic energy conversion.
(3) 3-D vortices and velocity streamlines at four different instants are examined for the TAEs operating at optimal r_h/δ_k at the steady state. The results indicate that the pin-array stack has a smaller flow resistance than the circular-pore stack.
(4) Accompanied by the vortex shedding, heat leaks are observed at the stack ends for both TAEs with circular-pore and pin-array stacks. The heat leaks lead to less heat involved in thermal-acoustic energy conversion and therefore reduce the thermal efficiency. The heat fluxes are higher at the surfaces of pin arrays than circular pores, revealing a superior performance in acoustic power generation for the TAE with a pin-array stack.

The 3-D CFD simulations conducted in this study give deeper insights into the performances of TAEs with circular-pore and pin-array stacks which were usually investigated in experiments. The numerical methodologies adopted in this research will provide valuable guidance for high-fidelity simulations of more advanced thermoacoustic devices such as thermoacoustic Stirling engines in the future.

CRediT authorship contribution statement

Geng Chen: Conceptualization, Methodology, Software, Validation, Formal analysis, Writing – original draft, Funding acquisition. **Shancheng Tao:** Methodology, Software, Validation, Formal analysis. **Kai Wang:** Writing – review & editing. **Lihua Tang:** Writing – review & editing, Supervision. **Zhaoyu Li:** Writing – review & editing. **Jingyuan Xu:** Writing – review & editing. **Zhibin Yu:** Writing – review & editing, Supervision.

Declaration of competing interest

The authors declare that they have no known competing financial interests or personal relationships that could have appeared to influence the work reported in this paper.

Data availability

Data will be made available on request.

Acknowledgments

This work is supported by the Natural Science Foundation of Jiangsu Province (Contract No. SBK2023041184), the Science and Technology R&D Program of China Railway Group Limited (2023-Major-23), and the Fundamental Research Funds for the Central Universities (Contract No. 2242023K40009, 2242023K30058, 2242023K30011). We would like to acknowledge the high-performance computing (HPC) provided by New Zealand eScience Infrastructure (NeSI).

Appendix. Validation against the linear thermoacoustic theory

The growth rate ω_I defined in Eq. (13) can also be predicted using the reduced-order network model based on the linear thermoacoustic theory. In the network model, the acoustic pressure p_1 and volume velocity U_1 at the left end ($x = 0$) and right end ($x = L$) of the TAE can be related by a transfer matrix $\mathbf{T_T}$,

$$\begin{bmatrix} p_1(x=L) \\ U_1(x=L) \end{bmatrix} = \mathbf{T_T} \begin{bmatrix} p_1(x=0) \\ U_1(x=0) \end{bmatrix} \tag{A1}$$

Detailed descriptions of the network model can be found in our previous study [27]. $\mathbf{T_T}$ contains thermal viscous functions for wide ducts, circular pores, and pin arrays, which are [1]

$$\begin{cases} f = \dfrac{(1-j)\delta}{2r_h}, Duct \\ f = \dfrac{2J_1[(j-1)2r_h/\delta]}{J_0[(j-1)2r_h/\delta](j-1)2r_h/\delta}, Circular\ pores \\ f \simeq \dfrac{2\alpha_i}{\alpha_0^2-\alpha_i^2}\dfrac{Y_1(\alpha_0)J_1(\alpha_i)-J_1(\alpha_0)Y_1(\alpha_i)}{Y_1(\alpha_0)J_0(\alpha_i)-J_1(\alpha_0)Y_0(\alpha_i)}, Pin\ arrays \end{cases} \tag{A2}$$

where J_0 and J_1 are the Bessel functions of order 0 and 1, Y_0 and Y_1 are the Neumann functions of order 0 and 1, $j = \sqrt{-1}$, and $\alpha = (j\text{-}1)/\delta$. Since U_1 at $x = 0$ and p_1 at $x = L$ are both zero, Eq. (A2) yields

$$T_{T11} = 0 \tag{A3}$$

where T_{T11} is the first element of matrix $\mathbf{T_T}$. Solving Eq. (A3) yields the eigenvalue (complex frequency $\omega = \omega_R + j\omega_I$) at any specified hot-end temperature T_H.

Fig. 17 shows the $\omega_{I,CFD}$ obtained from the CFD simulations and $\omega_{I,Linear}$ calculated from the network models at different T_H. Since the negative and positive ω_I indicate attenuation and amplification of acoustic oscillations respectively, the onset temperature for the TAE with a circular-pore stack is between 740 K and 755 K, which is larger than the onset temperature (between 580 K and 600 K) for the TAE with a pin-array stack. $\omega_{I,Linear}$ predicted using the linear theory are relatively larger than $\omega_{I,CFD}$ because CFD simulations account for the possible nonlinear viscous losses arising from vortices, streaming, etc. [39–41]. Overall, $\omega_{I,Linear}$ agrees well with $\omega_{I,CFD}$, demonstrating the validity of numerical and theoretical models constructed in the present work.

References

[1] G.W. Swift, Thermoacoustics: A Unifying Perspective for Some Engines and Refrigerators, Springer, 2017.
[2] G. Chen, L. Tang, B. Mace, Z. Yu, Multi-physics coupling in thermoacoustic devices: a review, Renew. Sustain. Energy Rev. 146 (2021) 111170.
[3] T. Jin, J. Huang, Y. Feng, R. Yang, K. Tang, R. Radebaugh, Thermoacoustic prime movers and refrigerators: thermally powered engines without moving components, Energy 93 (2015) 828–853.
[4] T. Biwa, M. Prastowo, E. Shoji, Thermoacoustic modeling of Fluidyne engine with a gas-coupled water pumping line, J. Acoust. Soc. Am. 152 (2022) 2212–2219.
[5] A. Maddi, C. Olivier, G. Poignand, G. Penelet, V. Pagneux, Y. Aurégan, Frozen sound: an ultra-low frequency and ultra-broadband non-reciprocal acoustic absorber, Nat. Commun. 14 (2023) 4028.
[6] K. Tsuda, Y. Ueda, Critical temperature of traveling-and standing-wave thermoacoustic engines using a wet regenerator, Appl. Energy 196 (2017) 62–67.
[7] S.-H. Hsu, Y.-T. Li, Estimation of limit cycle amplitude after onset threshold of thermoacoustic stirling engine, Exp. Therm. Fluid. Sci. (2023) 110956.
[8] G. Chen, J. Xu, Acoustic characteristics of looped-tube thermoacoustic refrigerators with external and in-built acoustic drivers: a comparative study, J. Acoust. Soc. Am. 150 (2021) 4406–4416.
[9] R. Yang, J. Wang, Z. Wu, B. Huang, E. Luo, Performance analysis of thermoacoustic plasma MHD generation, Energy (2022) 125647.
[10] S. Zhu, T. Wang, C. Jiang, Z. Wu, G. Yu, J. Hu, et al., Experimental and numerical study of a liquid metal magnetohydrodynamic generator for thermoacoustic power generation, Appl. Energy 348 (2023) 121453.
[11] A. Tavakolpour-Saleh, S. Zare, Justifying performance of thermo-acoustic Stirling engines based on a novel lumped mechanical model, Energy 227 (2021) 120466.
[12] R. Rahpeima, R. Ebrahimi, Numerical investigation of the effect of stack geometrical parameters and thermo-physical properties on performance of a standing wave thermoacoustic refrigerator, Appl. Therm. Eng. 149 (2019) 1203–1214.
[13] A. Piccolo, A.J. Jaworski, Experimental study of heat transfer characteristics of finned-tube and circular-pore heat exchangers in oscillatory flow, Appl. Therm. Eng. (2020) 116022.
[14] M. Hayden, G Swift, Thermoacoustic relaxation in a pin-array stack, J. Acoust. Soc. Am. 102 (1997) 2714–2722.
[15] M.A. Alamir, Experimental study of the stack geometric parameters effect on the resonance frequency of a standing wave thermoacoustic refrigerator, Int. J. Green. Energy (2019) 1–13.
[16] C. Wantha, The impact of stack geometry and mean pressure on cold end temperature of stack in thermoacoustic refrigeration systems, Heat Mass Transf. 54 (2018) 2153–2161.
[17] L. Gong, G. Penelet, P. Picart, Experimental and theoretical study of density fluctuations near the stack ends of a thermoacoustic prime mover, Int. J. Heat. Mass Transf. 126 (2018) 580–590.
[18] M. Tijani, J. Zeegers, A. De Waele, The optimal stack spacing for thermoacoustic refrigeration, J. Acoust. Soc. Am. 112 (2002) 128–133.
[19] Z. Yu, A. Jaworski, Optimization of thermoacoustic stacks for low onset temperature engines, Proc. Inst. Mech. Eng., Part A: J. Power Energy 224 (2010) 329–337.
[20] I. Farikhah, Y. Ueda, Numerical calculation of the performance of a thermoacoustic system with engine and cooler stacks in a looped tube, Appl. Sci. 7 (2017) 672.
[21] W.P. Arnott, H.E. Bass, R. Raspet, General formulation of thermoacoustics for stacks having arbitrarily shaped pore cross sections, J. Acoust. Soc. Am. 90 (1991) 3228–3237.
[22] N. Sugimoto, Nonlinear theory for thermoacoustic waves in a narrow channel and pore subject to a temperature gradient, J. Fluid. Mech. 797 (2016) 765–801.
[23] A. Piccolo, R. Siclari, F. Rando, M. Cannistraro, Comparative performance of thermoacoustic heat exchangers with different pore geometries in oscillatory flow. implementation of experimental techniques, Appl. Sci. 7 (2017) 784.
[24] H. Wang, B. Zhang, M. Liu, Z. Rao, Analytical solution of heat transfer performance of pin-array stack regenerator in stirling cycle, Int. J. Therm. Sci. 167 (2021) 107015.
[25] G. Swift, R. Keolian, Thermoacoustics in pin-array stacks, J. Acoust. Soc. Am. 94 (1993) 941–943.
[26] M. Jafari, A.J. Jaworski, A. Piccolo, K. Simpson, Numerical study of transient characteristics of a standing-wave thermoacoustic heat engine, Int. J. Heat. Mass Transf. (2022).
[27] G. Chen, L. Tang, Z. Yu, B. Mace, Mode transition in a standing-wave thermoacoustic engine: a numerical study, J. Sound. Vib. 504 (2021) 116119.
[28] D. Sun, K. Wang, Y. Guo, J. Zhang, Y. Xu, J. Zou, et al., CFD study on Taconis thermoacoustic oscillation with cryogenic hydrogen as working gas, Cryogenics 75 (2016) 38–46.
[29] C. Scalo, S.K. Lele, L. Hesselink, Linear and nonlinear modelling of a theoretical travelling-wave thermoacoustic heat engine, J. Fluid. Mech. 766 (2015) 368–404.
[30] G. Chen, L. Tang, B.R. Mace, Bistability and triggering in a thermoacoustic engine: a numerical study, Int. J. Heat. Mass Transf. 157 (2020) 119951.
[31] G. Harikumar, L. Shen, K. Wang, S. Dubey, F Duan, Transient thermofluid simulation of a hybrid thermoacoustic system, Int. J. Heat. Mass Transf. 183 (2022) 122181.
[32] S. Mergen, E. Yıldırım, H Turkoglu, Numerical study on effects of computational domain length on flow field in standing wave thermoacoustic couple, Cryogenics 98 (2019) 139–147.
[33] J. Luo, Q. Zhou, T. Jin, Numerical simulation of nonlinear phenomena in a standing-wave thermoacoustic engine with gas-liquid coupling oscillation, Appl. Therm. Eng. 207 (2022) 118131.
[34] F. Auriemma, E.D. Giulio, M. Napolitano, R. Dragonetti, Porous cores in small thermoacoustic devices for building applications, Energies 13 (2020) 2941.
[35] A. Di Meglio, N. Massarotti, CFD modeling of thermoacoustic energy conversion: a review, Energies 15 (2022) 3806.
[36] L. Hu, P. Yang, X. Lei, Y Liu, Numerical investigation on oscillations characteristics of self-excited thermoacoustic system forced by acoustic wave, Appl. Energy 315 (2022) 119028.
[37] M. Skaria, K.A. Rasheed, K. Shafi, S. Kasthurirengan, U. Behera, Simulation studies on the performance of thermoacoustic prime movers and refrigerator, Comput. Fluids 111 (2015) 127–136.
[38] P.J. Morris, S. Boluriaan, C.M. Shieh, Numerical simulation of minor losses due to a sudden contraction and expansion in high amplitude acoustic resonators, Acta Acustica United Acustica 90 (2004) 393–409.
[39] C. Yao, J. Liu, J. Yan, Numerical investigation of nonlinear effects in a standing wave thermoacoustic engine using the discontinuous Galerkin method, Int. J. Heat. Mass Transf. 216 (2023) 124526.
[40] G. Chen, H. Hao, A. Deng, Linear and nonlinear modeling of self-excited acoustic oscillations in a T-shaped thermoacoustic engine, AIP Adv. 11 (2021) 085120.
[41] M. Ja'fari, A.J. Jaworski, On the nonlinear behaviour of oscillatory flow in a high pressure amplitude standing-wave thermoacoustic heat engine, Int. J. Heat. Mass Transf. 201 (2023) 123595.